Disponible en www.hormigonyacero.com
Hormigón y Acero, 2026
https://doi.org/10.33586/hya.2026.4151

ARTÍCULO EN AVANCE ON LINE

Blast Resistance and Post-Cracking Performance of High-Strength Self-Compacting Fiber-Reinforced Concrete Slabs

David A. Cendón, Francisco Gálvez, Gonzalo Ruiz & Xiaoxin Zhang

DOI: https://doi.org/10.33586/hya.2026.4151

Para ser publicado en: *Hormigón y Acero*

Por favor, el presente artículo debe ser citado así:
Cendón, D.A., Gálvez, F., Ruiz, G., & Zhang, X. (2026) Blast Resistance and Post-Cracking Performance of High-Strength Self-Compacting Fiber-Reinforced Concrete Slabs, *Hormigón y acero*, https://doi.org/10.33586/hya.2026.4151

Blast Resistance and Post-Cracking Performance of High-Strength Self-Compacting Fiber-Reinforced Concrete Slabs

Comportamiento frente a explosiones y resistencia residual de losas de hormigón autocompactante de altas prestaciones reforzado con fibras de acero

David A. Cendón [(1)], Francisco Gálvez [(1)],
Gonzalo Ruiz [(2,*)] & Xiaoxin Zhang [(3)]

[(1)] ETSI Caminos, C. y P. — Universidad Politécnica de Madrid
Profesor Aranguren 3, 28040 Madrid, Spain

[(2)] ETSI Caminos, C. y P. — Universidad de Castilla-La Mancha
Avda. Camilo José Cela s/n, 13071 Ciudad Real, Spain

[(3)] Mining and Industrial Engineering School of Almadén — Universidad de Castilla-La Mancha, Plaza Manuel Meca, s/n, 13400 Almadén, Ciudad Real, Spain

[(*)] Correspondence: Gonzalo.Ruiz@uclm.es

March 3, 2026

Abstract

High-performance steel fiber-reinforced concrete (HPSFRC) is a promising material for structures subjected to dynamic loads, such as explosions. This study investigates the blast performance and residual strength of high-strength, self-compacting steel-fiber reinforced concrete slabs with different

fiber configurations. Three mixes were developed: Mix A with 40 kg/m^3 of straight 13 mm fibers, and Mixes B and C with additional 20 kg/m^3 and 40 kg/m^3 of hooked-end 30 mm fibers, respectively. Mechanical tests revealed distinct post-cracking behaviors and increasing fracture energy with fiber dosage. Blast tests showed that the higher fiber content improved crack control and structural integrity, with Mix C exhibiting minimal damage. Residual strength tests confirmed that Mix C retained both peak load and stiffness, while Mix B preserved load capacity but showed reduced stiffness. Mix A suffered significant degradation. These results highlight the role of fiber architecture in enhancing energy dissipation and blast resilience in concrete structures.

El hormigón de altas prestaciones reforzado con fibras de acero es un material prometedor para estructuras expuestas a cargas dinámicas como explosiones. Este estudio analiza el comportamiento frente a explosiones y la resistencia residual de losas de hormigón autocompactante de alta resistencia, reforzadas con diferentes configuraciones de fibras. Se desarrollaron tres mezclas: la A con 40 kg/m^3 de fibras rectas de 13 mm, y las mezclas B y C con 20 kg/m^3 y 40 kg/m^3 adicionales de fibras de 30 mm con extremos conformados, respectivamente. Los ensayos mecánicos mostraron comportamientos post-fisuración distintos y un aumento significativo de la energía de fractura con la dosificación y longitud de las fibras. Los ensayos con explosivos mostraron que un mayor contenido de fibras mejora el control de fisuras y la integridad estructural, siendo la mezcla C la que presentó menor daño. Los ensayos de resistencia residual confirmaron que las losas de la mezcla C conservaron tanto la capacidad de carga como la rigidez, mientras que la mezcla B mantuvo la carga máxima pero mostró una reducción en la rigidez. La mezcla A sufrió una degradación significativa. Estos resultados destacan el papel clave de la arquitectura de las fibras en la disipación de energía y la mejora del comportamiento estructural frente a explosiones.

Keywords: Blast-resistant concrete; High-performance steel fiber-reinforced concrete (HPSFRC); Fracture mechanics; Residual strength; High strain-rate behavior.

Palabras clave: Hormigón resistente a explosiones; Hormigón de altas prestaciones reforzado con fibras de acero (HPSFRC); Mecánica de fractura; Resistencia residual; Comportamiento a alta velocidad de deformación.

1 Introduction

The increasing frequency and severity of terrorist attacks worldwide have underscored the vulnerability of civil and transport infrastructure to explosive threats. Incidents targeting airports, railway and subway stations, bridges, and governmental buildings have resulted in catastrophic damage, often exacerbated by the progressive collapse of structural systems [1–3]. These events have prompted a surge in research aimed at improving the resilience of structural materials under impulsive loads, including blast and impact scenarios [3–8].

Fiber-reinforced concretes (FRCs) have emerged as a promising class of materials for enhancing the ductility, toughness, and energy absorption capacity of concrete structures. By incorporating discrete fibers into the cementitious matrix, FRCs can significantly improve post-cracking behavior, delay crack propagation, and increase resistance to dynamic loads. Among these, high-performance fiber-reinforced concretes (HPSFRCs) represent a notable advancement, combining high compressive strength with superior tensile and flexural performance [7–9].

HPSFRCs are typically formulated using optimized matrices with low water-to-cement ratios, fine aggregates, and mineral admixtures such as silica fume, along with steel, synthetic, or hybrid fibers. The mechanical performance of HPSFRCs is governed by several parameters, including fiber type, geometry, orientation, volume fraction, and the quality of the fiber-matrix interface [9, 10]. These materials have demonstrated exceptional behavior under quasi-static and low strain-rate conditions; however, their response under high strain rates —typical of blast and impact events— remains less understood.

Although some experimental studies have investigated the performance of HPSFRC structural elements under blast and impact loads [11–13], there is a notable gap in systematic material-level investigations that isolate the effects of fiber architecture on dynamic fracture behavior [14, 15]. Recent reviews have emphasized the need for deeper understanding of fiber-matrix interaction, strain-rate sensitivity, and energy dissipation mechanisms in HPSFRCs subjected to impulsive loads [10, 16].

This paper presents an experimental study aimed at characterizing the behavior of self-compacting HPSFRCs under blast loading, with a focus on fracture mechanics and residual strength. Three concrete mixes were developed with varying fiber types and dosages to induce distinct softening and hardening behaviors. Mechanical characterization included compressive strength, Young's modulus, Poisson's ratio, and specific fracture energy at two strain rates. Blast tests were conducted on slab specimens to evaluate damage patterns and structural response. Post-blast residual strength tests provided insight into the integrity and load-bearing capacity of the damaged slabs.

2 Materials

2.1 Concrete Mixes

In this study, three distinct high-performance fiber-reinforced concrete (HPSFRC) mixes —designated as Mixes A, B, and C— were developed to investigate the influence of fiber type and dosage on post-cracking softening behavior under dynamic loading conditions. All mixes shared a common high-performance cementitious matrix, while differing in the type and quantity of steel fibers incorporated.

The base matrix composition consisted of CEM I 42.5 R-SR Portland cement, silica fume, siliceous filler, fine sand (with a maximum particle size of 0.8 mm), coarse sand (2.0 mm), and water. The constituents were proportioned by weight in the following ratio: $1 : 0.12 : 0.35 : 1.21 : 1.27 : 0.38$, respectively. This mixing proportion was selected to ensure high compressive strength, low permeability, and enhanced fiber-matrix bond characteristics.

The primary variable among the mixes was the steel fiber configuration. Two commercially available fiber types were employed:

- Short, straight fibers (Bekaert OL 13/.20), with a length of 13 mm, a diameter of 0.30 mm, and an aspect ratio of 65.
- Long, hooked-end fibers (Bekaert RC 80/30 BP), with a length of 30 mm, a diameter of 0.38 mm, and an aspect ratio of 80.

Table 1 details the fiber dosage for each concrete type. To ensure an even distribution of the fibers, we gradually incorporated them into the mixture. This gradual process enabled the fibers to disperse individually once the matrix had achieved the optimal fluidity and a glossy appearance. Slump flow tests were conducted in accordance with the standard procedure [17] to evaluate the fresh-state workability of the mixes. The slump flow diameter was measured along two orthogonal directions, and the average values are reported in Table 2. A visual representation of the slump flow test is provided in Fig. 1.

Concrete types	Short fibers (kg/m^3)	Long fibers (kg/m^3)
A	40	—
B	40	20
C	40	60

Table 1: Steel fiber contents for each concrete mix.

The observed reduction in slump flow with increasing long fiber content reflects the well-documented trade-off between fiber reinforcement and workability.

Figure 1: Slump flow test.

Concrete types	Slump diameters (mm × mm)
A	700 × 700
B	660 × 670
C	570 × 570

Table 2: Slump flow diameters of fresh concrete mixes.

Mix C, with the highest hooked-end fiber dosage, exhibited the lowest flowability, indicative of increased internal friction and reduced matrix mobility. This behavior is critical in blast-resistant applications, where fiber architecture must balance mechanical performance with practical constructability.

2.2 Mechanical Properties

The mechanical characterization of the three HPSFRC mixes encompassed compressive strength, tensile strength, Young's modulus, Poisson's ratio, and specific fracture energy. These parameters were selected to evaluate both the quasi-static and dynamic response of the materials, with particular emphasis on post-cracking behavior and strain-rate sensitivity.

Compressive strength (f_c) and Young's modulus (E) were determined using four cylindrical specimens per mix, each measuring 150 mm in diameter and 300 mm in height, in accordance with ASTM C39 [18]. Poisson's ratio (ν) was derived from lateral and axial strain measurements during loading.

Flexural strength (f_{flex}) and specific fracture energy (G_F) were obtained from three-point bending tests on notched prismatic specimens of dimensions $100 \times 100 \times 450$ mm^3, following the RILEM TC 162-TDF recommendations [19]. To investigate the influence of strain rate on fracture energy, tests were conducted at four distinct loading velocities:

- 2.2 μm/s and 22 mm/s using a servohydraulic testing machine (Fig. 3a),
- 1.8 m/s and 2.7 m/s using a drop-weight impact device (Fig. 3b) [15, 20, 21].

For each velocity and mix, four specimens were tested to ensure statistical robustness.

Table 3 summarizes the mechanical properties obtained under quasi-static loading conditions. The results validate the effectiveness of the mix design strategy in producing distinct post-peak behaviors. Representative load-displacement curves for the three mixes at two loading rates are presented in Fig. 2, illustrating the transition from softening to hardening with increasing fiber content.

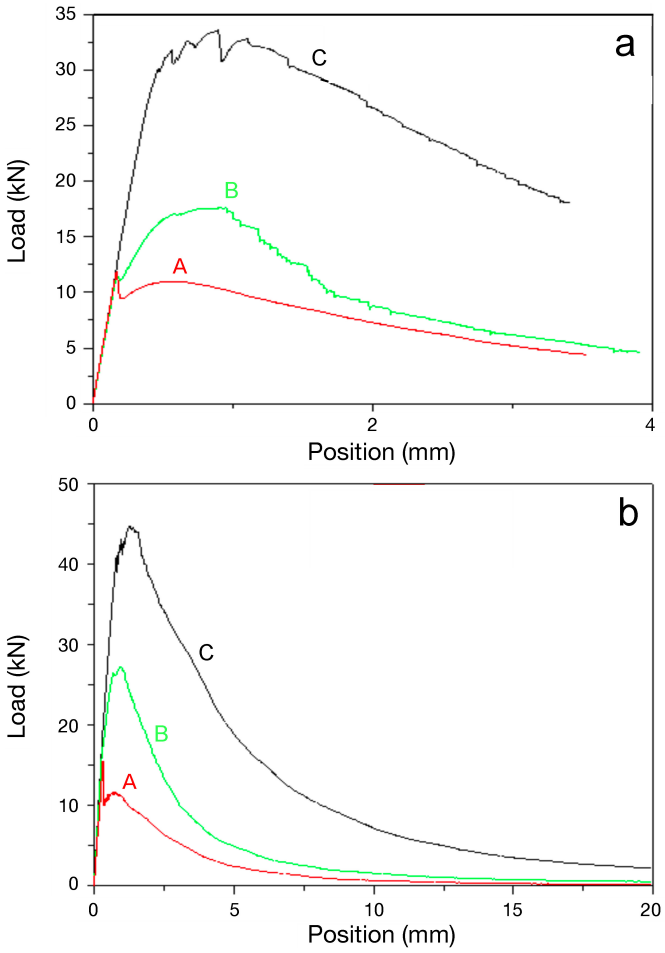

Figure 2: Load-displacement curves at loading velocities of: a) 2.2 μm/s; and b) 22 mm/s.

Following peak load —which marks the initiation of macrocrack propagation— Mix A (the lowest fiber content) exhibited a gradual decline in load-bearing capacity, characteristic of softening behavior. In contrast, Mix C (the highest fiber content) demonstrated a pronounced increase in load after cracking, indicative of strain-hardening. This behavior is attributed to the synergistic effect of high fiber dosage and the mechanical anchorage provided by hooked-end fibers. Mix B, with intermediate fiber content, displayed transitional behavior between the two extremes.

Concrete type	f_{flex} (MPa)	E (GPa)	ν	f_c (MPa)
A	8.5 (0.3)	46 (3)	0.18 (0.01)	112 (1)
B	14.8 (3)	45 (2)	0.17 (0.01)	113 (6)
C	25.3 (0.05)	46 (3)	0.17 (0.01)	114 (3)

Table 3: Mechanical properties of the concrete mixes (standard deviations in parenthesis).

Specific fracture energy was evaluated at a fixed displacement of 3 mm across all loading rates. Table 4 and Fig. 3c present the results, highlighting the influence of both fiber content and strain rate. A consistent trend was observed: fracture energy increased with fiber dosage at all displacement rates. For instance, Mix B exhibited approximately 60% higher energy absorption than Mix A, while Mix C showed increases of 200% and 125% over Mix A at low and high rates, respectively.

The effect of strain rate was quantified using dynamic increase factors (DIF), defined as the ratio of dynamic to quasi-static fracture energy. At the highest loading rate (2.7 m/s), DIF values were 2.81, 2.76, and 2.15 for Mixes A, B, and C, respectively. These results suggest that while all mixes benefit from rate-dependent toughening, the relative enhancement diminishes with increasing fiber content, likely due to saturation effects in fiber bridging mechanisms.

Concrete type	G_F (kN/m) for a δ of 3 mm at a $\dot{\delta}$ of:			
	2.2 μm/s	22 mm/s	1.8 m/s	2.7 m/s
A	3.07 (0.26)	3.78 (0.42)	8.06 (0.77)	8.63 (0.55)
B	5.06 (1.17)	6.17 (0.79)	12.35 (2.08)	13.96 (0.61)
C	9.41 (0.36)	12.55 (2.65)	17.75 (0.23)	20.22 (0.59)

Table 4: Fracture energies at 3 mm displacement for various loading rates (standard deviations in parentheses).

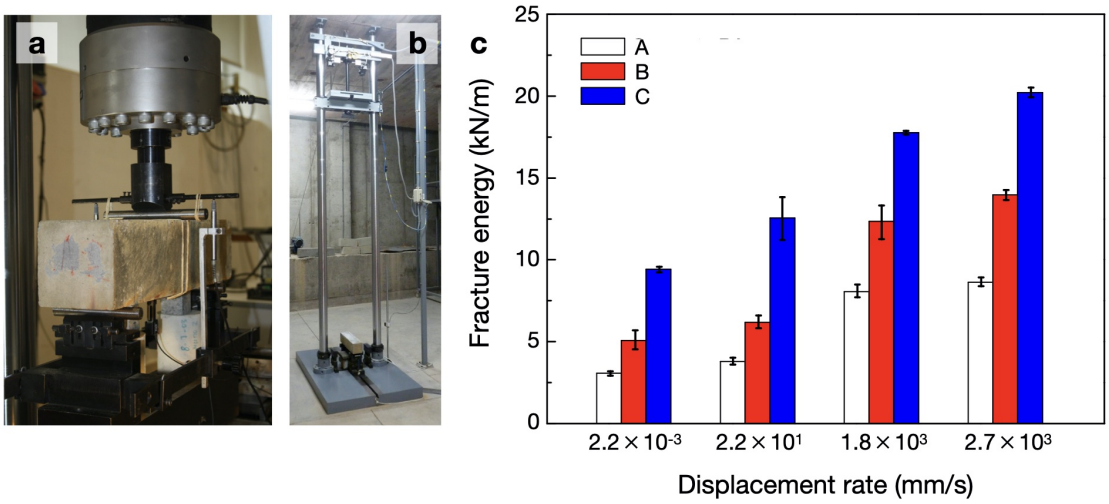

Figure 3: Fracture energy measurements at multiple displacement rates: (a) servo-hydraulic machine (2.2 μm/s and 22 mm/s); (b) drop-weight device (1.8 m/s and 2.7 m/s); (c) fracture energy vs. displacement rate for all mixes at $\delta = 3$ mm.

2.3 Blast Test Specimens

To evaluate the blast resistance of the fiber-reinforced concrete mixes described in Section 2.1, square slab specimens with nominal dimensions of $500 \times 500 \times 50$ mm^3 were fabricated. Each slab was cast using one of the three mix designs (A, B, or C), ensuring consistent curing and handling procedures across all specimens to minimize variability.

For each concrete type, six slabs were fabricated, resulting in a total of eighteen specimens. Of these, four slabs per mix were selected for blast testing, while the remaining two were reserved for post-blast analysis and control comparisons. Note that we did not consider plain concrete slabs since they would likely have fragmented into numerous pieces under the blast loads considered, making their characterization impractical. Since such slabs are unsuitable for protective purposes, our study focuses instead on the influence of different fiber reinforcements.

The slab geometry was chosen to realistically assess damage mechanisms like spalling, cracking, and fiber pull-out under high-strain-rate loading conditions. It is important to note that the slab geometry used in this study is not intended to represent full-scale protective elements. It can also be used to calibrate numerical models for modelling this type of concrete under blast loading. This approach is commonly adopted when the primary objective is to investigate the fracture and post-cracking behavior of high-performance fiber-reinforced concretes under impulsive actions. Additionally, since high-performance fiber-reinforced concretes

have long characteristic lengths (calculated as $\ell_{ch} = G_F E/f_t^2$), indicating their high ductility, size effects were not considered. This suggests that significant size effects can be negligible, as noted in [22].

Additionally, the slabs used in the experiments were approximately twice as thick as the length of the long fibers (Bekaert RC 80/30 BP, which are 30 mm long). Consequently, the long fibers were largely aligned with the free surfaces of the slabs, potentially creating a wall effect that enhances slab bending. This wall effect would diminish in thicker slabs.

3 Blast Tests

3.1 General Characteristics

The blast tests were conducted following the standardized procedure described in [23, 24], employing a purpose-built steel frame test bench designed to ensure uniform exposure of specimens to the blast load. As illustrated in Fig. 4, the square steel frame was capable of accommodating up to four concrete slabs per detonation, thereby enabling simultaneous testing under identical loading conditions.

Figure 4: Test bench used in the blast tests.

Each slab was simply supported at its corners within the frame, allowing for free deformation and minimizing boundary constraints. This configuration ensured that the blast pressure was uniformly distributed across the exposed surface of each slab, facilitating consistent damage assessment and comparative analysis.

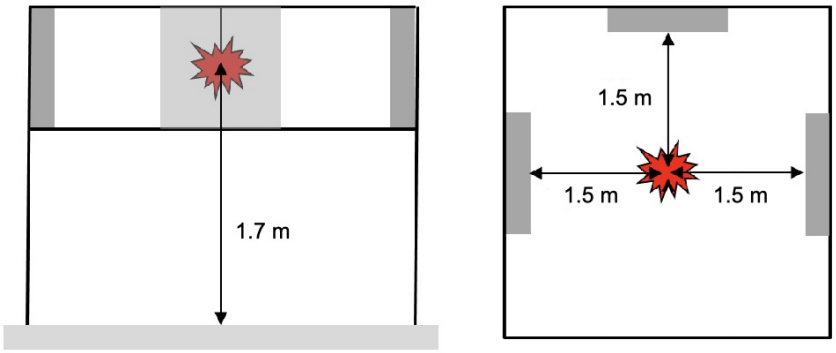

Figure 5: Sketch and dimensions of the test bench.

The steel frame featured a column spacing of 3.00 m, establishing a stand-off distance of 1.50 m between the explosive charge and the slab surfaces. To reduce the influence of ground-reflected shock waves and enhance the fidelity of the pressure field, the explosive was elevated to a height of 1.70 m above the ground. A schematic representation of the test bench, including its geometric configuration and spatial layout, is provided in Fig. 5.

All detonations employed Goma-2 ECO, a commercial dynamite-class explosive manufactured by Maxam. The explosive was supplied in cylindrical cartridges, each containing 151.5 g of active material. The TNT equivalence of Goma-2 ECO —based on the ratio of the heat of explosion of both explosives per unit weight— is 0.956, which can be used to calibrate the blast energy and estimate the equivalent charge mass for comparative analysis. For initiation, we used RIONEL LP non-electric detonators and RIONEL LLX shock tubes.

3.2 Testing Procedure

To enable a direct and controlled comparison of the blast performance among the three concrete mixes, each detonation involved one slab from each mix type. This setup resulted in three slabs being tested for every detonation (see Figs. 4 and 5). By using this configuration, we minimized variability caused by spatial or temporal differences during the explosive events. Each slab was identified by a name that includes a letter corresponding to the mix type (A, B, or C) followed by a number ranging from 1 to 6. Table 5 presents the slabs that served as references for the residual strength tests (Test 0) and those that were subjected to the blast loading. Importantly, in all cases, the rough side of the slab, which was exposed during the forming process, faced the blast wave.

An initial calibration test was conducted using 17 cartridges of Goma-2 ECO,

corresponding to an explosive mass of approximately 2.58 kg (Test 1). This preliminary trial served to verify the functionality of the data acquisition system and to provide a baseline assessment of slab damage under moderate blast loading. As the resulting damage was limited, the explosive charge was subsequently increased to 22 cartridges, yielding a total mass of 3.33 kg of Goma-2 ECO.

To account for inherent variability in concrete properties and blast testing conditions, the final test configuration was repeated three times (Tests 2-4). This ensured that each concrete mix was represented by three specimens exposed to the same blast load, thereby enhancing the statistical reliability of the results. The explosive configurations employed throughout the test campaign are summarized in Table 5.

The cartridges were arranged in a bunch, roughly resembling a cylinder. Figure 6a depicts one of these cartridges' bunch positioned in front of a slab, while Fig. 6b presents a view of the cartridges from below. The image also depicts the detonating cord penetrating the center of the bunch to initiate the explosion.

All detonations were documented using a high-speed camera. Figure 7 presents a sequence of frames captured during Test 4, with each image annotated to indicate the elapsed time relative to detonation. Rey *et al.* [24] showed that this blast setup leads to an approximately spherical blast front and that the pressure distribution across the slab surfaces is effectively uniform, which is also suggested by the recorded movies (see Fig. 7).

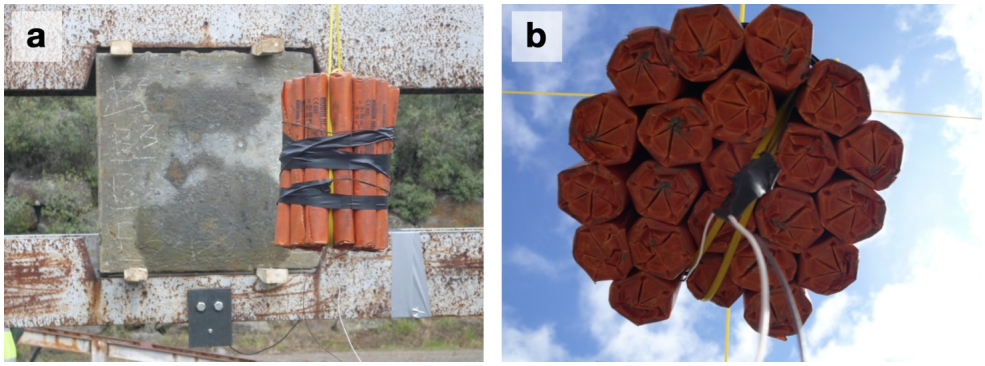

Figure 6: Details of the explosive arrangement: (a) A bunch of cartridges positioned in front of the slab of concrete B before Test 3 (the image also depicts the pressure sensor, supported by a plate fixed to the frame); and (b) a bottom-view detail of the cartridge bunch.

Test	N° of cartridges	Goma 2 (kg)	TNT eqv. (kg)	slab name		
0	—	—	—	A1, A2	B4, B5	C1, C2
1	17	2.58	2.46	A4	B2	C4
2				A3	B3	C3
3	22	3.33	3.18	A6	B6	C6
4				A5	B1	C5

Table 5: Explosive loads and concrete types tested.

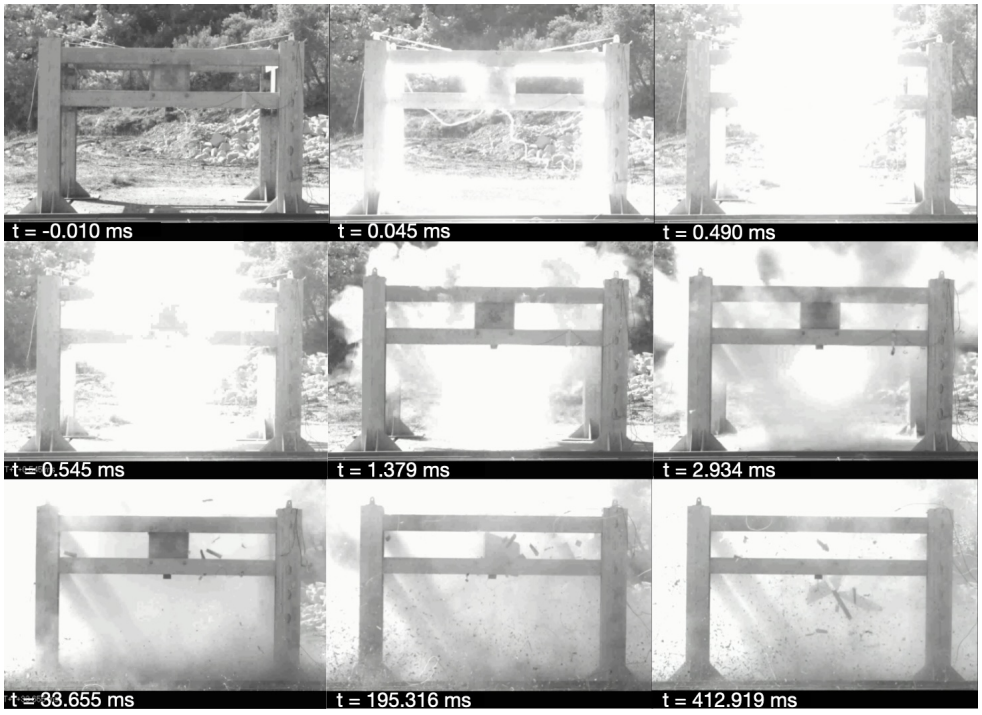

Figure 7: Snapshots of the Test 4, captured by the high-speed camera.

3.3 Blast Pressure Histories

To support subsequent numerical simulations and to validate empirical blast load models, pressure-time histories acting on the concrete slabs were recorded during each detonation. For this purpose, a PCB Piezotronics 102B piezoelectric pressure transducer was positioned right below one of the slabs (see Fig. 6a) to capture the incident pressure wave generated by each detonation. The acquisition system operated at a sampling frequency of 25 MHz. This setup enabled precise quantification of key blast wave parameters, including peak overpressure, specific impulse, and positive phase duration. The instrumentation was calibrated to ensure minimal signal distortion and accurate synchronization with the detonation event.

As illustrated in Fig. 8, the recorded pressure histories demonstrated good consistency across the three 3.33 kg Goma-2 ECO blasts (Tests 2-4). This repeatability confirms the reliability of the test configuration and the uniformity of the explosive charge deployment, thereby reinforcing the validity of the pressure data for use in computational modeling and comparative analysis.

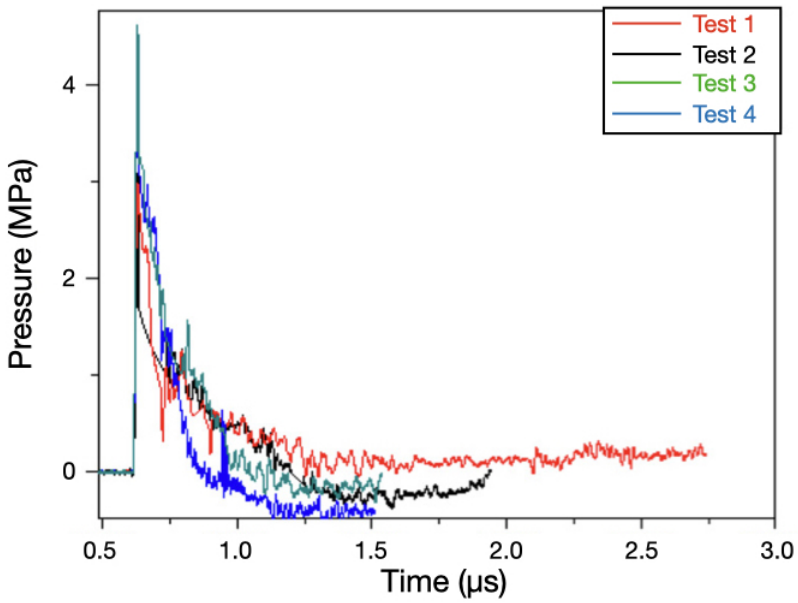

Figure 8: Blast pressure histories recorded during the tests.

3.4 Results and Discussion

3.4.1 Overall Behavior of the Slabs

Figure 9 displays the concrete slabs immediately following Test 2, arranged in ascending order of fiber content from bottom to top. It shows the rough side for concretes B and C, while the smooth surface is visible in the case of concrete A. Note that, in all blast tests, the rough surface of each slab —the face that remained free during casting— was consistently oriented toward the explosive charge. This ensured a uniform and reproducible exposure condition across all specimens, and facilitated the observation of the crack patterns in the tensioned smooth surface.

The visual inspection of post-blast damage reveals a clear correlation between fiber dosage and the structural response of the slabs, underscoring the critical role of fiber content and geometry in mitigating blast-induced damage. The slab fabricated with the lowest fiber content (Mix A) exhibited extensive cracking and partial fragmentation, indicating that the energy dissipated through crack propagation was insufficient to preserve structural integrity. Detached concrete fragments were observed, particularly on the tensioned surface, suggesting limited post-cracking load transfer capacity and inadequate fiber bridging.

In contrast, the slab constructed with the highest fiber content (Mix C) — incorporating both a greater volume of fibers and longer, hooked-end fibers— demonstrated superior blast resistance. Only minor surface cracking was visible on the tensioned face, and the opposite face remained largely intact, with no signs of spalling or delamination. This behavior reflects enhanced energy absorption and crack control mechanisms facilitated by the dense and mechanically anchored fiber network.

The slab corresponding to the intermediate fiber content (Mix B) exhibited damage characteristics between those of Mixes A and C. While visible crack patterns were present, the slab retained its overall structural coherence, with no significant material loss. This transitional response highlights the progressive improvement in blast resilience with increasing fiber reinforcement.

3.4.2 Failure Patterns

The post-blast failure patterns of the concrete slabs were systematically documented and analyzed (see Fig. 10). The photos displayed in the figure were taken in the laboratory before testing them to evaluate the residual mechanical behavior. All the images show the smooth surface that was in contact with the mold, which was consistently the tensioned face during the blasts. The crack patterns were more pronounced on this side, as the openings of the cracks were wider.

Across all specimens, the observed crack trajectories predominantly exhibited characteristics of shear failure, with curved cracks forming around the slab sup-

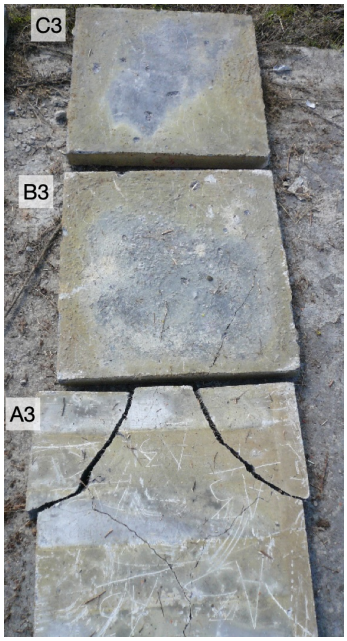

Figure 9: Slabs after Test 2.

ports. This failure mode is consistent with the stress concentration zones induced by the blast wave and the boundary conditions of the test setup.

When compared to previous experimental campaigns using fiber-reinforced concretes with substantially lower fiber contents [25, 26], the current specimens demonstrated markedly more distributed cracking. Figure 11 juxtaposes the crack patterns from the present study with those obtained in [25, 26]. Although both campaigns employed similar blast loads and self-compacting fiber-reinforced concrete formulations, the earlier study incorporated 25 kg/m^3 of long fibers, whereas the present investigation utilized a minimum fiber dosage of 40 kg/m^3. This substantial increase in fiber content not only enhanced the mechanical strength of the material but also induced strain-hardening behavior, which facilitated stress redistribution and promoted the formation of multiple cracks across a broader slab area.

A comparative analysis of the crack patterns between Mixes A and B reveals a higher crack density in Mix B. This phenomenon is attributed to the more pronounced hardening response of Mix B, as evidenced by its post-peak load-displacement behavior (see Fig. 2a). Although both mixes exhibited similar resistance to crack initiation —reflected in the comparable peak loads— the ability of Mix B to sustain and increase load beyond the initial cracking point enabled the development of additional crack surfaces. In contrast, Mix A, lacking significant

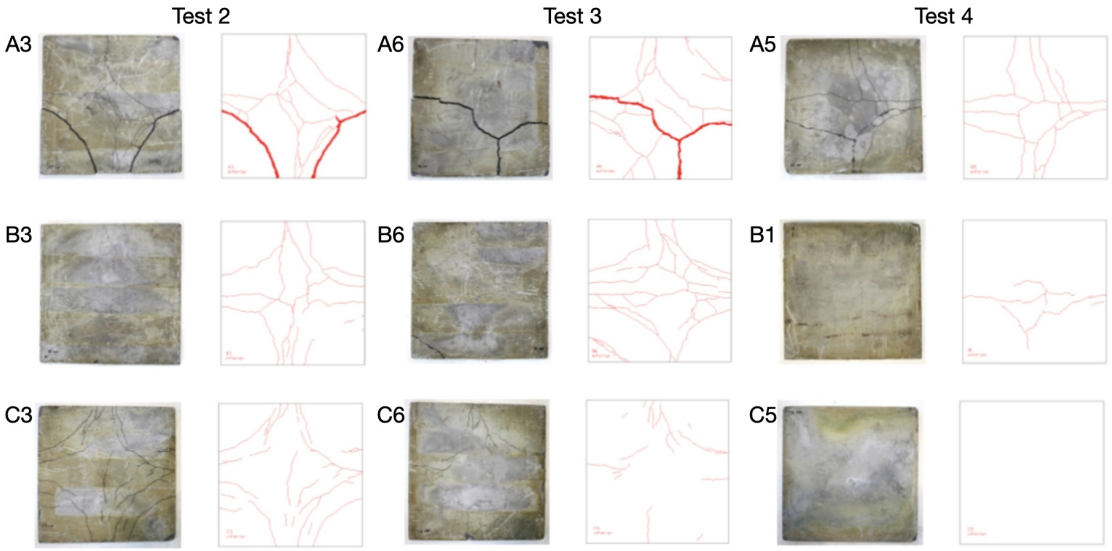

Figure 10: Crack patterns observed on the surface opposite to the blast wave in all the slabs of Tests 2-4.

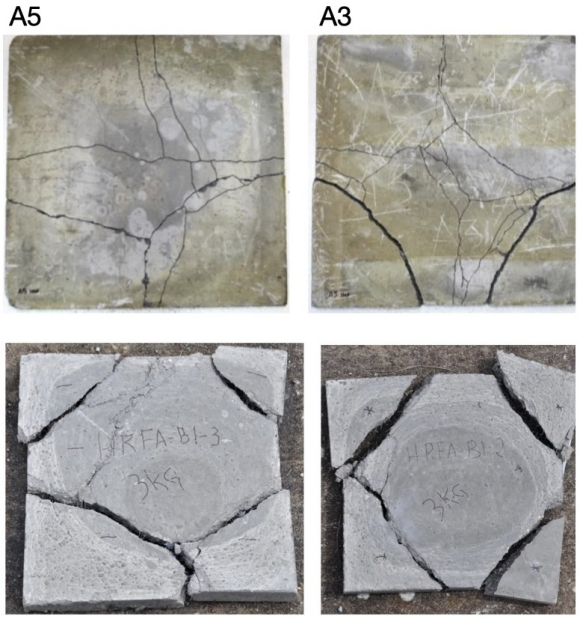

Figure 11: Comparison of crack patterns: concrete A from the present study (upper row) and a similar slab from [25, 26] (lower row).

post-peak strength gain, exhibited fewer but more localized cracks.

Mix C, characterized by the highest fiber content and superior resistance to crack initiation, displayed the lowest crack density among the three. The enhanced tensile capacity of Mix C, combined with its robust strain-hardening behavior, limited the propagation of cracks and preserved the structural coherence of the slab under blast loading.

These observations underscore the energy dissipation mechanisms inherent to fiber-reinforced concretes. The elevated specific fracture energies measured in the mechanical characterization phase, coupled with the ability to redistribute stresses, facilitated the generation of new crack surfaces. This process significantly increased the total energy absorption capacity of the slabs, contributing to their improved blast resistance.

4 Residual Strength of Slabs

4.1 Test Setup

To evaluate the post-blast structural capacity of the fiber-reinforced concrete slabs, residual flexural strength tests were conducted under quasi-static loading conditions. These tests included both slabs previously subjected to blast loading and two untested reference slabs from each concrete mix, enabling direct comparison between damaged and intact specimens.

The initial testing protocol proposed a five-point bending configuration, with the load applied centrally and the slabs supported at their corners. However, visual inspection following the blast tests revealed extensive damage at the slab corners (see Figs. 9 and 10), which compromised the integrity of the support points. Consequently, the test configuration was revised to a three-line bending setup, as illustrated in Fig. 12. This alternative arrangement provided stable support and allowed for reliable measurement of flexural response.

During testing, the applied load and mid-span vertical displacement were continuously recorded using two linear variable differential transformers (LVDTs). All tests were performed using a servo-hydraulic testing machine with a maximum capacity of 1 MN, operating at a controlled displacement rate of 7 μm/s to ensure quasi-static conditions.

Due to the severity of blast-induced damage, two slabs from Mix A (A3 and A6) were rendered unsuitable for retesting. To supplement the dataset and enhance the robustness of the analysis, slabs previously exposed to the preliminary blast load (17 cartridges) were included in the residual strength evaluation. These specimens provided valuable intermediate data points between fully intact and severely damaged slabs.

Figure 12: Experimental setup for the tests of the residual strength of the slabs.

4.2 Results and Discussion

Figure 13 presents the load-average displacement curves obtained from the residual strength tests conducted on both intact and blast-damaged slabs, and Table 6 arrays the average values of the load peaks, the flexural strengths, and the fracture energies measured from the curves.

Several key observations can be drawn from these curves. First, regarding peak load capacity —and consequently flexural strength— only the slabs fabricated with Mix A showed a noticeable reduction after blast exposure. This trend is supported by the comparative data from Table 6 plotted in Fig. 14. Specifically, the peak load of slab A4 (subjected to 17 cartridges) was significantly lower than that of the intact reference slabs (A1 and A2), but it remained higher than the peak load recorded for slab A5 (subjected to 22 cartridges). This gradual decrease in peak load with increasing blast intensity highlights the vulnerability of low-fiber concrete to explosive damage.

	Peak load (kN)	f_{flex} (MPa)	G_F (kN/m)
A	28.6 (0.2)	10 (0.3)	3.23 (0.01)
A (17)	24.7	8.2	2.35
A (22)	9	3	0.62
B	50.5 (7.5)	15.8 (0.9)	5.47 (0.4)
B (17)	43.2	12.76	4.52
B (22)	52.1 (3.7)	15.6 (1.1)	4.68 (0.2)
C	61.2 (0.4)	21.5 (0.6)	7.04 (0.01)
C (17)	55.8	19.2	6.40
C (22)	65.7 (5)	21.87 (1.4)	7.06 (0.7)

Table 6: Peak loads, flexural strengths, and fracture energies obtained in the slabs' tests (standard deviations in brackets for results coming from several slabs).

In contrast, slabs constructed with Mixes B and C did not exhibit any appreciable reduction in peak load following blast exposure. This suggests that the higher fiber content and improved post-cracking behavior of these mixes effectively preserved their load-bearing capacity under quasi-static conditions, even after severe dynamic loading.

Beyond peak load, the effect of blast loading on structural stiffness is also evident. Both Mixes A and B showed reductions in initial stiffness following detonation, whereas Mix C remained largely unaffected. In the case of Mix B, the high fiber reinforcement content induces a delayed peak in the load-displacement response, even in intact specimens. This behavior implies that while the ultimate load capacity remains intact, the concrete matrix suffers internal damage that manifests as a reduction in stiffness.

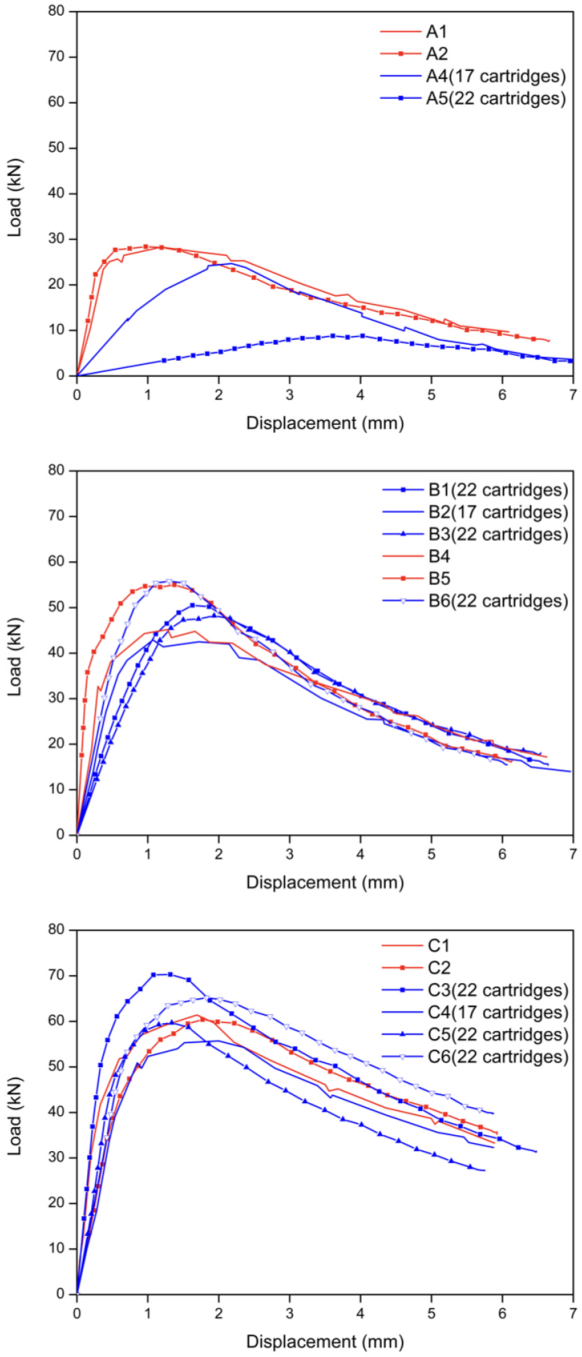

Figure 13: Load-displacement curves of the intact and blast-damaged slabs.

It is important to note that while peak load governs the ultimate bearing capacity of a structural element, stiffness plays a critical role in stress distribution within a structural system. A sudden loss of stiffness following blast exposure can lead to unintended stress redistribution, potentially triggering progressive collapse mechanisms. Therefore, stiffness degradation should be considered a key parameter in the design and assessment of blast-resistant structures.

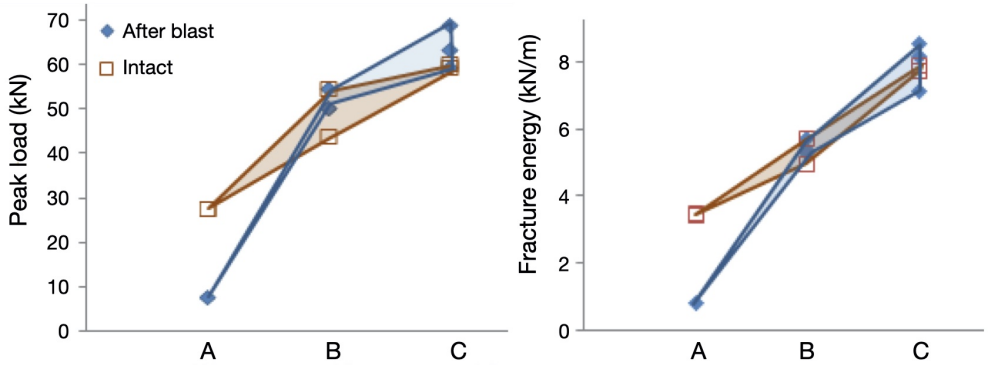

Figure 14: Comparison of the peak loads and fracture energies measured in the pristine and tested slabs for all concrete types.

The fracture energies from the tests on the slabs indicate that slabs made from Mix A are significantly damaged, as the residual fracture energy is only 20% of that of the intact slabs. In contrast, slabs made from Mixes B and C show no reduction in energy consumption, which confirms that they maintain their functionality after the blast. It is important to note that the noticeable increase in ductility in the slabs of Mix B does not appear to affect the fracture energy significantly, since this improvement is likely attributed more to the fibers than to the matrix itself [27, 28].

5 Conclusions

This study presented an experimental investigation into the blast behavior and post-cracking performance of high-performance self-compacting concrete reinforced with steel fibers. Three fiber-reinforced concrete mixes —designated as A, B, and C— were developed with varying fiber types and dosages to induce distinct softening and hardening behaviors.

Comprehensive mechanical characterization, including compressive and tensile strength, Young's modulus, and specific fracture energy at multiple strain rates, confirmed the effectiveness of the mix design strategy. The results demonstrated that increasing fiber content and incorporating hooked-end fibers significantly en-

hanced strain-hardening behavior and energy dissipation capacity. Mix C, with the highest fiber dosage and longest fibers, exhibited superior fracture resistance and dynamic toughness.

Blast tests conducted on slab specimens revealed a strong correlation between fiber architecture and damage mitigation. Mix A, with the lowest fiber content, suffered fragmentation and structural compromise, while Mix C maintained integrity with minimal visible cracking. Mix B displayed intermediate behavior, validating the progressive improvement in blast resilience with increased fiber reinforcement.

Post-blast failure pattern analysis showed that higher fiber contents promoted distributed cracking and stress redistribution, reducing the likelihood of localized failure. Comparisons with previous campaigns using lower fiber dosages highlighted the critical role of fiber-induced strain-hardening in enhancing blast resistance.

Residual strength tests further underscored the importance of fiber reinforcement. While Mix A exhibited a clear reduction in peak load and stiffness after blast exposure, Mixes B and C retained their load-bearing capacity. Notably, Mix B showed stiffness degradation despite unchanged peak strength, indicating internal matrix damage. These findings emphasize that stiffness loss —often overlooked— can critically affect load redistribution and contribute to progressive collapse in structural systems.

In summary, the results demonstrate that fiber type, dosage, and geometry are decisive factors in improving the blast resilience and post-cracking performance of concrete. The enhanced fracture energy, distributed failure mechanisms, and retained residual strength observed in high-fiber mixes position them as promising materials for protective infrastructure applications. Future work will expand on these findings through dynamic residual strength testing and numerical modeling to further inform design strategies for blast-resistant concrete structures.

Funding

This research received funding from the *Ministerio de Innovación, Ciencia y Universidades*, Spain, through grant PID2023-147971OB-C31, *Junta de Comunidades de Castilla-La Mancha*, Spain, through grant SBPLY/24/180225/000003, and *Universidad de Castilla-La Mancha* & ERDF through grant 2025-GRIN-38445.

References

[1] B.R. Ellingwood. Mitigating risk from abnormal loads and progressive collapse. *Journal of Performance of Constructed Facilities*, 20(4):315–323, 2006.

[2] D.O. Dusenberry. *Handbook for Blast Resistant Design of Buildings*. John-Wiley & Sons, 2010.

[3] E. Cadoni, A. Pérez Caldentey, M. Colombo, A.N. Dancygier, M. di Prisco, H. Grisaro, P. Martinelli, J. Ožbolt, M. Pajak, and Jaap Weerheijm. State-of-the-art on impact and explosion behaviour of concrete structures: report of RILEM TC 288-IEC. *Materials and Structures*, 58(2):62, 2025.

[4] T.T. Garfield, W.D. Richins, T.K. Larson, C.P. Pantelides, and J.E. Blakeley. Performance of RC and FRC wall panels reinforced with mild steel and GFRP composites in blast events. *Procedia Engineering*, 10:3534–3539, 2011.

[5] M. Mára, C. Talone, R. Sovják, J. Fornusek, J. Zatloukal, P. Kheml, and P. Konvalinka. Experimental investigation of thin-walled UHPFRCC modular barrier for blast and ballistic protection. *Applied Sciences*, 10(23):8716, 2020.

[6] R.R. Castedo, A.P. Santos, A. Alanón, C. Reifarth, M. Chiquito, L.M. López, S. Martínez-Almajano, and A. Pérez-Caldentey. Numerical study and experimental tests on full-scale RC slabs under close-in explosions. *Engineering Structures*, 231:111774, 2021.

[7] Rizwanullah and H.K. Sharma. Blast loading effects on UHPFRC structural elements: A review. *Innovative Infrastructure Solutions*, 7(6):341, 2022.

[8] A. Měrkováa, P. Khemla, A. Perrotb, and P. Hálaa. Experimental investigation of polyurethane-coated HPFRC panels under direct contact blast. *Acta Polytechnica*, 65(2):188–197, 2025.

[9] T.E.T. Buttignol, J.L.A.O. Sousa, and T.N. Bittencourt. Ultra high-performance fiber-reinforced concrete (UHPFRC): A review of material properties and design procedures. *IBRACON Structures and Materials Journal*, 10:957–971, 2017.

[10] J. Trajano da Silva Neto, P.R. Ribeiro Soares Jr., E. Dias Reis, P. de Souza Maciel, P.C. Correia Gomes, A.M.C. Gouveia, and A. Cesar da Silva Bezerra. Fiber-reinforced cementitious composites: Recent advances and future perspectives on key properties for high-performance design. *Discover Civil Engineering*, 2(65), 2025.

[11] G. Morales, J. Magnusson, H. Hansson, A. Ansell, F. Gálvez, and V. Sánchez-Gálvez. Behaviour of concrete structural members subjected to air blast loading. In *Ballistics 2013*, pages 1–12. 27$^{\text{th}}$ International Symposium on Ballistics, Freiburg, 2013.

[12] J. Xu, C. Wu, H. Xiang, Y. Su, Z.-X. Li, Q. Fang, H. Hao, Z. Liu, Y. Zhang, and J. Li. Behaviour of ultra high performance fibre reinforced concrete columns subjected to blast loading. *Engineering Structures*, 118:97–107, 2016.

[13] M. Foglar, R. Hajek, J. Fladr, J. Pachman, and J. Stoller. Full-scale experimental testing of the blast resistance of HPFRC and UHPFRC bridge decks. *Construction and Building Materials*, 145:588–601, 2017.

[14] P. Bibora, M. Drdlová, V Prachař, and O. Sviták. UHPC for blast and ballistic protection, explosion testing and composition optimization. *IOP Conference Series: Materials Science and Engineering*, 251(1):012004, 2017.

[15] X.X. Zhang, G. Ruiz, M. Tarifa, D. Cendón, F. Gálvez, and W.H. Alhazmi. Dynamic fracture behavior of steel fiber reinforced self-compacting concretes (SFRSCCs). *Materials*, 10(11):1270, 2017.

[16] V. Anish and J. Logeshwari. A review on ultra high-performance fibre-reinforced concrete with nanomaterials and its applications. *Journal of Engineering and Applied Science*, 71(25), 2024.

[17] ASTM C1611/C1611M-21. *Standard Test Method for Slump Flow of Self-Consolidating Concrete*. Annual Book ASTM Standards, 2021.

[18] ASTM C39-21. *Standard test method for compressive strength of cylindrical concrete specimens*. Annual Book ASTM Standards, 2021.

[19] RILEM TC 162 TDF. Test and design methods for steel fibre reinforced concrete. $\sigma - \epsilon$ design method. Final recommendation. *Materials and Structures*, 36(8):560–567, 2003.

[20] X.X. Zhang, G. Ruiz, R.C. Yu, and M. Tarifa. Fracture behaviour of high-strength concrete at a wide range of loading rates. *International Journal of Impact Engineering*, 36(10):1204–1209, 2009.

[21] X.X. Zhang, G. Ruiz, and R.C. Yu. A new drop-weight impact machine for studying fracture processes in structural concrete. *Strain*, 46:252–257, 2010.

[22] Z.P. Bažant and J. Planas. *Fracture and Size Effect in Concrete and Other Quasibrittle Materials*. CRC Press, Boca Raton, Florida, 1998.

[23] G. Morales-Alonso, D. A. Cendón, F. Gálvez, B. Erice, and V. Sánchez-Gálvez. Blast response analysis of reinforced concrete slabs: Experimental procedure and numerical simulation. *Journal of Applied Mechanics*, 78(5):051010, 2011.

[24] V. Rey, F. Gálvez, R. Sancho, and D.A. Cendón. Experimental procedure for testing concrete slabs under blast loading. *Proceedings*, 2(8):459, 2018.

[25] M. Oña. *Estudio experimental de elementos de protección de hormigón armado sometidos a explosiones*. Master Thesis. Ingeniería de las Estructuras, Cimentaciones y Materiales. Universidad Politécnica de Madrid, 2014.

[26] M. Oña, G. Morales-Alonso, F. Gálvez, V. Sánchez-Gálvez, and D. Cendón. Analysis of concrete targets with different kinds of reinforcements subjected to blast loading. *The European Physical Journal Special Topics*, 225(5):265–282, 2016.

[27] M. Tarifa, E. Poveda, V.M.C.F. Cunha, and J.A.O. Barros. Effect of the displacement rate and inclination angle in steel fiber pullout tests. *International Journal of Fracture*, 223:109–122, 2020.

[28] E. Poveda, R.C. Yu, M. Tarifa, G. Ruiz, V.M.C.F. Cunha, and J.A.O. Barros. Rate effect in inclined fibre pull-out for smooth and hooked-end fibres: A numerical study. *International Journal of Fracture*, 223:135–149, 2020.